Catalysis Today 462 (2026) 115548

Contents lists available at ScienceDirect

Catalysis Today

journal homepage: www.elsevier.com/locate/cattod

Effect of A-site substitution for Pt supported $La_{0.8}A_{0.2}FeO_3$ perovskite for aqueous-phase aerobic oxidation of ethylene glycol to glycolic acid using O_2

Seungdon Kwon, Nagyeong Kim, Hyeonji Yeom, Hanbit Jang, Kyungsu Na *

Department of Chemistry, Chonnam National University, Gwangju 61186, Republic of Korea

ARTICLE INFO

Keywords:
Ethylene glycol
Glycolic acid
Perovskite
Pt catalyst
Oxidation
Oxygen vacancy

ABSTRACT

Selective oxidation of biomass-derived polyols into value-added chemicals is a promising strategy for sustainable chemical production. Among these, ethylene glycol (EG) serves as a versatile platform molecule due to its simple structure and dual hydroxyl functionality. In this study, a series of perovskite-type oxides with the general formular of $La_{0.8}A_{0.2}FeO_3$ (A = Mg, Ca, Sr, Ba) was synthesized and impregnated with 1 wt% Pt to investigate structure–activity relationships in the aerobic oxidation of EG to glycolic acid (GA). Physicochemical characterizations using XPS, H_2-TPR, O_2-TPO, and ethanol chemisorption revealed that A-site substitution significantly affected Pt dispersion, oxidation state, and oxygen vacancy concentration. Notably, Sr-substituted catalysts exhibited high EG conversion and GA selectivity under both pressurized and ambient conditions, which was attributed to the presence of metallic Pt^0, abundant oxygen vacancies, facile oxygen activation, and enhanced interaction with –OH containing reactants. These findings propose the critical role of A-site engineering in tailoring perovskite-supported Pt catalysts and provide valuable insights into the rational design of heterogeneous oxidation catalysts for polyol upgrading.

1. Introduction

The global push toward the carbon neutrality has intensified the search for sustainable alternatives to fossil-based resources [1,2]. As awareness of climate change and environmental degradation continues to grow, renewable feedstocks such as biomass have garnered significant attention for their potential to replace conventional petrochemicals in both energy production [3] and chemical manufacturing [4,5]. Biomass is not only carbon-neutral but also rich in structurally diverse compounds that can be upgraded into valuable fuels and chemicals through catalytic processes [6,7]. Polyols, which are polyhydric alcohols containing multiple hydroxyl groups, have emerged as versatile platform molecules among biomass-derived compounds [8,9], with examples such as glycerol, sorbitol, and ethylene glycol (EG) typically obtained through the hydrolysis or hydrogenolysis of lignocellulosic biomass [10–12]. Owing to their multifunctionality, these compounds offer various opportunities for catalytic valorization into fine chemicals, solvents, and monomers [13–18].

In particular, EG has attracted substantial industrial and academic interest due to its wide availability, chemical simplicity, and broad applicability [18–20]. Compared to other polyols, relatively simple structure of EG—with two hydroxyl groups—facilitates mechanistic investigations and selective catalytic control. Catalytic upgrading of EG can proceed through several pathways, including reforming [18,21,22], dehydrogenation [23,24], and oxidation [25–33]. Among these, selective oxidation is especially promising, as it enables direct transformation of hydroxyl groups into carboxylic acids or aldehydes, which are key intermediates in the production of biodegradable polymers, cosmetics, and pharmaceuticals [26–33]. Depending on the reaction conditions and catalyst design, EG oxidation can yield a range of products such as oxalic acid (OA), formic acid (FA), glycolaldehyde, and glycolic acid (GA), the latter of which is a high-value C_2 compound with widespread commercial utility [29–33]. Therefore, developing efficient catalytic systems for the selective oxidation of EG to GA is of significant importance.

Noble metal-based heterogeneous catalysts have been widely utilized for the oxidation of EG, owing to their high activity and tunable selectivity under relatively mild conditions [26–33]. Numerous studies have demonstrated that both the oxidation state and dispersion of noble metal particles significantly influence catalytic performance, with the

* Corresponding author.
E-mail address: kyungsu_na@chonnam.ac.kr (K. Na).

https://doi.org/10.1016/j.cattod.2025.115548
Received 15 July 2025; Received in revised form 26 August 2025; Accepted 2 September 2025
Available online 8 September 2025

metallic state often identified as the active site for oxidative dehydrogenation [31–34]. Among these systems, Pt-based catalysts have recently received particular attention, as Pt offers a superior balance between activity, selectivity, and stability in aqueous phase oxidation, making it especially effective for EG-to-GA transformation (Table 1) [31–33]. Beyond the intrinsic properties of noble metal, the choice of support material has also emerged as a crucial design parameter. Traditional oxide supports like TiO_2, CeO_2, Al_2O_3, and carbon have been used to stabilize noble metal nanoparticles, control their dispersion, and modulate the metal–support interface [26–30]. However, recent research has highlighted that the inherent redox property and the oxygen activation capability of the support can also directly contribute to catalytic turnover, especially in oxidation reactions where lattice oxygen or oxygen vacancies play an active role in the reaction mechanism [14,15,28,31]. For instance, Pt/Mn_2O_3 and Pt/NaY systems have demonstrated enhanced activity for EG oxidation through electronic and structural synergies at the Pt–support interface [31–33]. In the Pt–Mn_2O_3 system, strong metal–oxide interactions not only promote high Pt dispersion but also facilitate surface oxygen exchange, leading to improved selectivity to GA [31]. Similarly, Pt/NaY catalysts with tailored $(Si–OH)_n$–Pt interfacial motifs stabilize isolated Pt^0 atoms, which are proposed to enhance C–H and O–H bond activation through σ-complex formation [32]. Moreover, single-atom Pt catalysts coordinated with PO_4^{3-} species have been reported to exhibit outstanding selectivity in EG oxidation by restricting over-oxidation and stabilizing key intermediates [33]. These examples highlight that optimizing EG oxidation requires more than achieving high Pt dispersion: rational control of the Pt–support interface, including the ability of supporting materials for activating molecular oxygen and generating oxygen vacancies, are essential for maximizing catalytic performance. Consequently, integrating active noble metal sites with redox-active supports emerges as a promising strategy for the selective and efficient valorization of biomass-derived polyols such as ethylene glycol.

In this regard, perovskite oxides (ABO_3-type structures) can be attractive choices for support because of their structural flexibility, adjustable redox property, and strong metal–support interaction [34–47]. In these materials, A-site cations primarily stabilize the lattice, while B-site transition metals provide redox activity. Among them, La-based perovskites with transition metal B sites have received considerable attention due to their robustness and versatile catalytic properties. An additional advantage of perovskites is their compositional tunability at both the A- and B-sites, allowing for fine control over their electronic structure, oxygen mobility, and surface properties—factors that are highly relevant to oxidation catalysis [38–43,46,47]. Substitution of the A-site with divalent alkaline-earth metal ions can further generate oxygen vacancies through charge compensation, thereby enhancing lattice oxygen dynamics. These characteristics make perovskites particularly promising support for noble metals such as Pt, where synergistic interactions between the metal nanoparticle and the redox-active lattice can be exploited to enhance both activity and selectivity. Despite this potential, the effect of A- and B-site modifications on catalytic performance of Pt/perovskite systems—and the associated structure–activity relationships—remain largely unexplored in the selective oxidation of EG to GA.

In this study, we investigate a series of Pt-loaded perovskite catalysts based on $LaBO_3$ (B = Cr, Mn, Fe, and Co) and $La_{0.8}A_{0.2}BO_3$ (A = Mg, Ca, Sr, and Ba), focusing on their structural, redox, and surface chemical properties in relation to their activity and selectivity for EG oxidation to GA. Lanthanum was selected as the A-site cation for its structural stability and compatibility with various B-site transition metals, while Cr, Mn, Fe, and Co were chosen to represent diverse redox properties. Partial substitution of La with alkaline earth metals was introduced to modulate lattice strain and oxygen vacancy concentration via charge compensation. The La:A ratio of 0.8:0.2 was selected to ensure sufficient incorporation of the substituent cations while avoiding phase instability or solubility-limit issues, thereby enabling a fair comparison among different A-site cations. By combining catalytic testing with X-ray photoelectron spectroscopy, temperature-programmed oxidation, and ethanol chemisorption, we elucidate how perovskite composition governs Pt dispersion, oxygen vacancy, and oxygen activation capability. Our findings highlight A-site substitution as an effective strategy for optimizing metal–support interactions and enhancing catalytic performance in base-assisted ethylene glycol oxidation.

2. Experimental

2.1. Materials preparation

2.1.1. Chemicals

All chemicals used in this work were commercially available and used without further purification. The chemicals used in this work are platinum chloride ($PtCl_4$, 99.5 %, DAEJUNG, 6767–4150), lanthanum nitrate hexahydrate ($La(NO_3)_3·6\ H_2O$, 99.9 %, DAEJUNG, 5062–8805), chromium nitrate nonahydrate ($Cr(NO_3)_3·9\ H_2O$, 98 %, DAEJUNG, 2555–4405), manganese nitrate hexahydrate ($Mn(NO_3)_2·6\ H_2O$, 97 %, Junsei Chemical, 37585S1201), iron nitrate nonahydrate ($Fe(NO_3)_3·9\ H_2O$, 98 %, DAEJUNG, 5023–4405), cobalt nitrate hexahydrate ($Co(NO_3)_2·6\ H_2O$, 98 %, Sigma-Aldrich, 230375), magnesium nitrate hexahydrate ($Mg(NO_3)_2·6\ H_2O$, 98 %, DAEJUNG, 5508–4405), calcium nitrate tetrahydrate ($Ca(NO_3)_2·4\ H_2O$, 98 %, Junsei Chemical, 37405S1201), strontium nitrate ($Sr(NO_3)_2$, 98 %, DAEJUNG, 7669–4405), barium nitrate ($Ba(NO_3)_2$, 99 %, Sigma-Aldrich, 217581), citric acid monohydrate ($C_6H_8O_7·H_2O$, 99.5 %, Junsei Chemical, 26040S0301), and ethyl alcohol (C_2H_5OH, 95 %, DAEJUNG, 4119–4410).

2.1.2. Preparation of Pt supported La-based perovskite (Pt/$LaBO_3$ or Pt/$La_{0.8}A_{0.2}BO_3$)

A typical synthesis involved dissolving 0.01 mol each of La $(NO_3)_3·6\ H_2O$ and $B(NO_3)_x·yH_2O$, (B= Cr, Mn, Fe, Co; x = 2, 3, y = 6, 9), along with 8.4 g (0.04 mol) of citric acid, in 100 mL of ethanol. The resulting solution was stirred under reflux for 1 h and then evaporated overnight in an oven at 90 °C. The obtained residue was ground into a fine powder and calcined at 700 °C for 5 h under air flow to yield the $LaBO_3$ perovskite materials. $La_{0.8}A_{0.2}BO_3$ were synthesized in the same manner, except that 0.008 mol of La precursor and 0.002 mol of A-site nitrate (A = Mg, Ca, Sr, and Ba) were used instead.

The conventional wet impregnation method was employed to prepare 1 wt% Pt supported catalysts. An aqueous solution of $PtCl_4$ (5.177×10^{-4} M) was prepared and added to the perovskite support

Table 1
Summary of the performances of the catalysts developed in this study and those of representative reported catalysts for EG oxidation.

Entry	Catalyst	Condition	EG Conversion (%)	Selectivity (%)						Ref.
				GA	GAL	GO	GOA	OA	FA	
1	1Pt/$La_{0.8}Sr_{0.2}FeO_3$	60 °C, 1 MPa O_2, 4 h, NaOH	95.8	82.2	-	-	-	7.1	10.7	This work
2	1Pt/$La_{0.8}Sr_{0.2}FeO_3$	60 °C, 0.1 MPa O_2, 8 h, NaOH	56.6	80.0	-	-	-	0.9	19.1	This work
3	Pt-Fe/CeO_2	70 °C, 1 MPa O_2, 12 h, NaOH	100	62	-	-	-	9	8	[28]
4	PtMn/MCM−41	60 °C, 1 MPa O_2, 8 h	92.1	93.8	2.5	-	-	-	0.1	[31]
5	Pt/NaY	70 °C, 1 MPa O_2, 10 h	97.7	77.6						[32]
6	Pt_1/HAP	50 °C, 1 MPa O_2, 16 h, NaOH	79.1	98.3	-	-	-	-	0.2	[33]

under vigorous stirring at room temperature. The mixture was stirred for 2 h, followed by evaporation and drying overnight at 100 °C. The obtained residue was ground into a fine powder and calcined at 550 °C for 3 h under air flow.

2.2. Materials characterization

X-ray diffraction (XRD) patterns were collected using a Rigaku MiniFlex 600 instrument with a Cu Kα radiation (λ = 0.1541 nm) operated at 600 W (40 kV, 15 mA). The measurements were performed under ambient conditions with a step size of 0.02 °, scanning rate of 3 ° min^{-1}, and a 2θ range of 20–70°. N_2 adsorption/desorption analysis was conducted using a BELSORP MAX II volumetric analyzer. Prior to analysis, sample was degassed at 400 °C under vacuum for 3 h. The analysis was then performed at a liquid nitrogen temperature (77 K). The specific surface area and pore size were calculated according to the Brunauer–Emmett–Teller (BET) theory and Barrett–Joyner–Halenda (BJH) method, respectively. The crystal morphologies were examined using transmission electron microscopy (TEM) imaging. TEM images were acquired using a JEM–2100 F (JEOL Ltd.) with a spherical aberration corrector operated at 200 kV. The content of Pt in the catalysts was determined via inductively coupled plasma-optical emission spectroscopy (ICP-OES; Avio 500, PerkinElmer, Waltham, MA, USA). H_2 temperature-programmed reduction (TPR) and O_2 temperature programmed oxidation (TPO) measurements were conducted using a BEL–CAT II (BEL JAPAN INC) equipped with mass (MS) detector. Prior to the H_2-TPR measurements, perovskite samples were pre-treated under an Ar stream for 1 h at 400 °C in a quartz cell to degas the adsorbed species. The samples were then cooled to 50 °C. The samples were treated with 10 % H_2/Ar flows with increasing cell temperatures from 50 to 950 °C at a ramping rate of 10 °C min^{-1} and then maintaining the temperature at 950 °C for 30 min, while the exhaust gas was analyzed using thermal conductivity detector (TCD) and MS. Prior to O_2-TPO measurement, 1Pt/$La_{0.8}A_{0.2}BO_3$ perovskite samples were pre-treated under 5 % H_2/He stream for 1 h at 400 °C in a quartz cell to degas the adsorbed species and reduced the Pt species. The samples were then cooled to 50 °C and purged with He for 30 min. The samples were treated with 5 % O_2/He flows with increasing cell temperatures from 50 to 650 °C at a ramping rate of 10 °C min^{-1} and then maintaining the temperature at 650 °C for 30 min, while the exhaust gas was analyzed using TCD and MS. XPS was performed using a K–ALPHA+ instrument (Thermo Fisher Scientific, Waltham, MA, USA) equipped with a monochromatic Al Kα source connected to a 128–channel detector. Prior to the measurements, all investigated catalysts were reduced under H_2/Ar flows of 50 mL min^{-1} at 400 °C for 3 h using a ramping rate of 5 °C min^{-1}. The peak binding energy was calibrated by the C 1 s peak position (284.8 eV), corresponding to the surface hydrocarbon-like deposits. The XPS spectra were analyzed by fitting Gaussian–Lorentzian curves after baseline correction. For the ethanol pulse adsorption, 0.05 g of catalyst was pretreated under 5 % H_2/He flows of 30 mL min^{-1} for 1 h at 400 °C. When the temperature was cooled to 50 °C with He purge for 30 min, ethanol molecule was pulsed into the quartz tube. The flask and reflux temperatures of ethanol steam generator were 50 and 40 °C. Three consecutive peaks show the same peak area, indicating that the sample test is completed. An ethanol/Pt stoichiometry of 2.5 obtained from the molecule size ratios was used to calculate the adsorptive ratios [31].

2.3. Reaction studies

2.3.1. Pressurized batch reaction

The reactor setup is shown in Fig. S1a. Catalytic performance was evaluated using a 110 mL Teflon-lined stainless-steel autoclave reactor. Prior to the reaction, the Pt supported catalyst was pretreated with H_2 under a flow of Ar and H_2 at 400 °C for 3 h. For the reaction, 0.1 g catalyst was added to 30 mL of 0.3 M EG solution containing 1.5 g of NaOH for basic environment. The reactor was purged with O_2 to remove residual air and then pressurized to 10 bars with O_2. The reactor was heated to 60 °C and stirred at 600 rpm for 4 h. After the reaction, the reactor was rapidly cooled in an ice bath, and the catalyst was separated from the solution using a syringe filter. A 2 mL of liquid of the reaction solution was immediately mixed with 2 mL of 1 M H_2SO_4 solution for neutralization before analysis.

2.3.2. Atmospheric pressure reaction

The atmospheric-pressure reaction setup is illustrated in Fig. S1b. In a 100 mL three-neck flask, 0.1 g of catalyst was added to 30 mL of 3 M EG aqueous solution containing 1.5 g of NaOH. The mixture was stirred and heated to 60 °C using a heating mantle, and the system was equipped with an overhead condenser for temperature stability. Molecular O_2 was bubbled into the aqueous solution at a flow rate of 60 standard mL/min. At specific intervals, 1 mL of the reaction mixture was taken, neutralized with H_2SO_4, and analyzed by high-performance liquid chromatography to obtain concentration-time profiles.

2.3.3. Product analysis and quantification

High-performance liquid chromatography (HPLC, Perkin-Elmer UC/200) was employed to analyze the liquid-phase products. Ethanol was used as an internal standard. A refractive index detector and a Bio-Rad Aminex HPX-87H column were used, with 0.005 M H_2SO_4 as the mobile phase. The conversion of EG and the selectivity of products were calculated using the following equations:

$$\text{Conversion}\ (\%) = 100 - \frac{EG_0 - EG_t}{EG_0} \times 100$$

$$\text{Product selectivity}\ (\%) = \frac{Product_t}{\sum Product_t} \times 100$$

Here, EG_0 and EG_t represent the concentrations of EG at the initial stage and after reaction time t, respectively, while $Product_t$ is the concentration (mol/L) of a specific product formed after time t.

3. Results and discussion

3.1. Physicochemical properties of perovskite materials

X-ray diffraction (XRD) patterns of the synthesized $LaBO_3$ (B = Cr, Mn, Fe, Co) samples are shown in Fig. S2 and their structural property including surface areas, measured by N_2 adsorption/desorption analysis (Fig. S3), are shown in Table S1. All samples exhibit distinct and sharp diffraction peaks, which are characteristic of well-crystallized perovskite-type structures. The observed peak positions match well with those reported for orthorhombic or rhombohedral perovskite phases [38–45], depending on the B-site cation, indicating successful formation of the intended ABO_3 framework without detectable secondary phases. Notably, the diffraction peak positions and relative intensities vary slightly among the samples, which can be attributed to differences in ionic radius and electronic configurations of the transition metals occupying the B-site of ABO_3 structure [38–40]. For instance, $LaCoO_3$ displays features consistent with rhombohedral symmetry [38,41,42], while $LaCrO_3$, $LaMnO_3$ and $LaFeO_3$ show patterns typically associated with orthorhombic distortions [38,39,43,44,45]. This structural adaptability of the perovskite framework enables it to incorporate various B-site cations while maintaining its crystallographic phase stability. To evaluate their applicability as oxidation catalysts, 1 wt% of Pt was impregnated onto each perovskite. The corresponding XRD patterns of the Pt-loaded samples are presented in Fig. 1a and 1b. The diffraction patterns of the perovskite phase remained unchanged after Pt incorporation. Furthermore, no distinct diffraction peaks corresponding to metallic Pt or PtO_x phases were observed, which suggests that Pt species were highly dispersed across the perovskite surface.

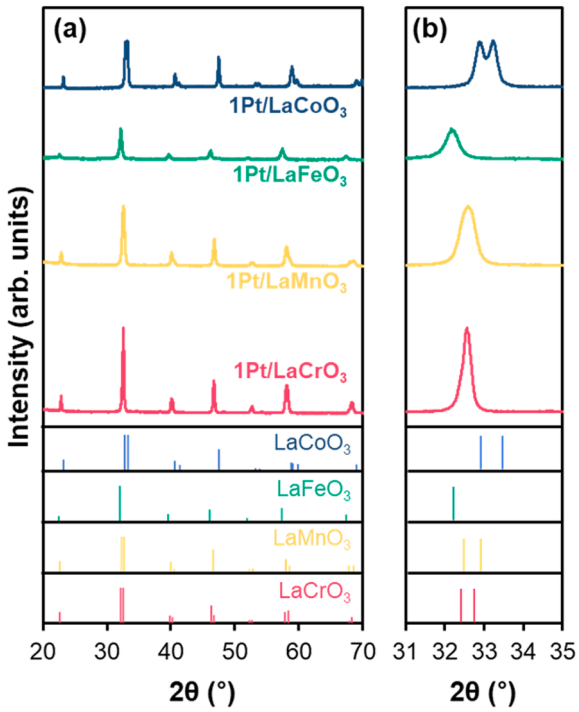

Fig. 1. (a) XRD patterns and (b) their magnified view in the 2θ region of 31–35° of 1Pt/$LaCrO_3$ (red), 1Pt/$LaMnO_3$ (yellow), 1Pt/$LaFeO_3$ (green), and 1Pt/$LaCoO_3$ (blue) with vertical (hkl) lines indicating peaks corresponding to each perovskite from the JCPDS database.

The morphological characteristics of the 1 wt% Pt-impregnated perovskite catalysts were examined by TEM, as shown in Fig. 2. The images show Pt nanoparticles uniformly dispersed across the perovskite surface, with no visible agglomeration. The average particle sizes were 1.12 ± 0.23 nm (1Pt/$LaCrO_3$), 1.28 ± 0.16 nm (1Pt/$LaMnO_3$), 2.47 ± 0.73 nm (1Pt/$LaFeO_3$), and 1.35 ± 0.30 nm (1Pt/$LaCoO_3$) (inset histograms in the magnified TEM images in Fig. 2). These results indicate a clear variation in Pt dispersion depending on the B-site composition of the perovskite, with 1Pt/$LaFeO_3$ showing relatively larger and more broadly distributed Pt particles. In contrast, 1Pt/$LaCrO_3$ and 1Pt/$LaMnO_3$ exhibited smaller and more narrowly distributed nanoparticles. The TEM images are consistent with the XRD results (Fig. 1a), which showed no distinguishable diffraction peaks corresponding to bulk Pt crystals. These observations collectively indicate that Pt is well dispersed in the form of small nanoparticles, as supported by the absence of distinct Pt peaks in XRD and the nanoscale distribution observed in TEM. ICP-OES analysis confirmed that the actual Pt loading was within 0.96–1.07 wt% (Table S2).

The impregnation of Pt did not significantly alter the perovskite crystal structure; however, its electronic characteristics, particularly reducibility, were markedly affected, as evidenced by the H_2-TPR profiles of the $LaBO_3$ series (Fig. 3). The reduction behavior of the pristine perovskites varied significantly depending on the B-site cation, reflecting intrinsic differences in their redox properties. For $LaCrO_3$, a small reduction peak around 420 °C can be attributed to the reduction of Cr (VI) to Cr(III), likely associated with a minor La_2CrO_6 phase [34]. In case of $LaMnO_3$, two peaks at 377 and 472 °C were observed, corresponding to the removal of the non-stoichiometric excess lattice oxygen and partial reduction of Mn(IV) to Mn(III). A broader peak at around 800 °C is attributed to the reduction of Mn(III) to Mn(II) [35]. For $LaFeO_3$, a low-temperature peak at 340 °C could be assigned to the reduction of adsorbed oxygen species, while the second peak at 492 °C was attributed to the reduction of surface Fe(IV) to Fe(III) and Fe(III) to Fe(II) [36]. In case of $LaCoO_3$, reduction peaks appeared in two areas around 400–500 °C and 550–650 °C. The former could be associated with Co(III) to Co(II) while the latter could be related to Co(II) to metallic Co [36]. Upon Pt loading, notable changes appeared in the reduction profiles, including shifts in peak positions and the emergence of new low-temperature peaks. These newly formed low-temperature peaks are primarily attributed to the reduction of initially oxidized platinum species (PtO_x) to metallic Pt, which typically occurs below 200 °C [31–33]. 1Pt/$LaMnO_3$ and 1Pt/$LaCoO_3$ show prominent peaks at 191 °C and 188 °C, respectively, indicating a substantial presence of oxidized Pt species. In contrast, 1Pt/$LaCrO_3$ and 1Pt/$LaFeO_3$ exhibited comparatively smaller peaks at 176 °C and 166 °C, respectively. This suggests

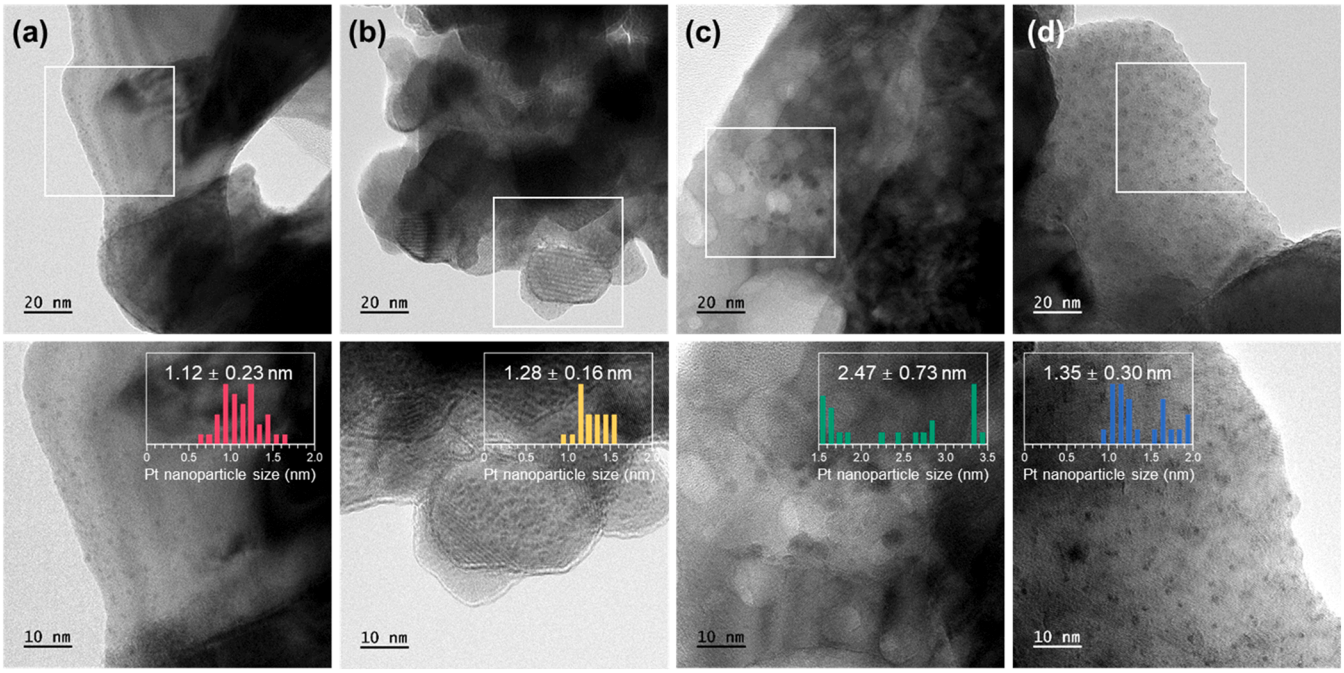

Fig. 2. TEM image of (a) 1Pt/$LaCrO_3$, (b) 1Pt/$LaMnO_3$, (c) 1Pt/$LaFeO_3$, and (d) 1Pt/$LaCoO_3$ with magnified view (bottom row) and the corresponding histograms of Pt nanoparticle size distribution.

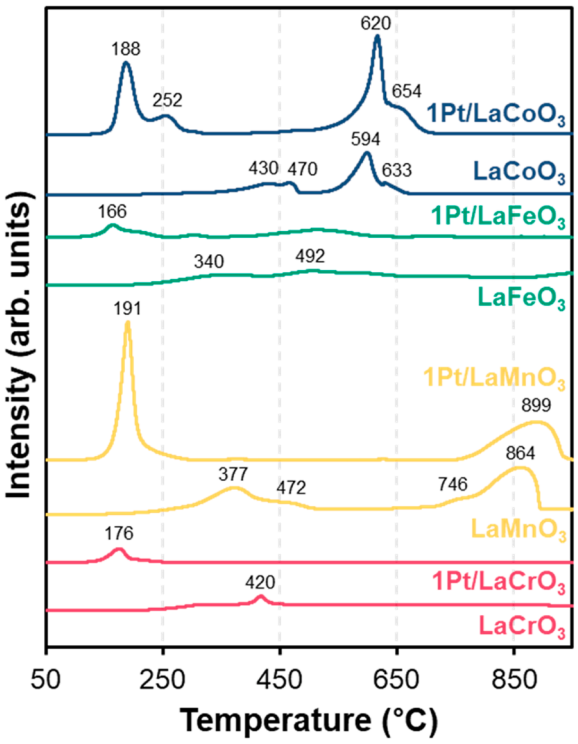

Fig. 3. H_2-TPR profiles of $LaBO_3$ (B = Cr, Mn, Fe, and Co) series and 1Pt/$LaBO_3$ series.

that a greater proportion of Pt exists in a metallic state even before the H_2 treatment, resulting in a smaller amount of reducible PtO_x. This interpretation was further supported by XPS analysis conducted on the catalysts before the H_2 treatment (Fig. S4 and Table S3), which confirmed a relatively higher proportion of metallic Pt in 1Pt/$LaCrO_3$ and 1Pt/$LaFeO_3$ compared to the other samples. Furthermore, the lower reduction temperatures imply that electron transfer to PtO_x is more facile in these perovskites. As observed in the H_2-TPR profiles in Fig. 3, the pristine perovskites exhibited markedly different hydrogen consumption behaviors depending on the B-site composition. In particular, 1Pt/$LaFeO_3$ and 1Pt/$LaCrO_3$ showed significantly lower reduction intensities than 1Pt/$LaMnO_3$ and 1Pt/$LaCoO_3$ (Fig. 3), which can be attributed to their ability to stabilize metallic Pt species on the surface, as supported by the pre-reduction XPS results (Fig. S4). Given that metallic Pt is generally regarded as the active phase for EG oxidation, $LaFeO_3$ and $LaCrO_3$ were selected as the base compositions for subsequent A-site substitution experiments to further optimize the catalytic performance.

Building upon the compositional flexibility of the perovskite framework, further structural tuning was achieved by partially substituting the A-site cation. While lanthanum ion (La^{3+}) was initially fixed as the A-site ion to maintain a consistent perovskite structure, subsequent modifications involved aliovalent substitution of La with alkaline earth metals such as Mg^{2+}, Ca^{2+}, Sr^{2+}, and Ba^{2+}, resulting in $La_{0.8}A_{0.2}BO_3$-type compositions. This strategy enables more precise control over lattice strain and unit cell symmetry, which in turn can influence redox properties and potentially the concentration of oxygen vacancies via charge compensation mechanisms [40–43,46,47]. Figs. 4a and S6 shows the XRD patterns of the synthesized $La_{0.8}A_{0.2}BO_3$ (A = Mg, Ca, Sr, Ba and B = Cr, Fe) samples. Despite A-site substitution, no significant structural changes were observed, suggesting that the overall perovskite framework was preserved. Nonetheless, slight shifts in diffraction peak positions were detected, likely due to local structural distortions arising from the ionic radius mismatch between La^{3+} and the substituted A-site cations. These subtle variations suggest that the physicochemical properties of each perovskite material were modulated by the A-site substitution.

The H_2-TPR spectra of the 1Pt/$La_{0.8}A_{0.2}FeO_3$ series reveal distinct variations in redox behavior depending on the A-site cations, as shown in Fig. 4c. Compared to 1Pt/$LaFeO_3$, the Mg-substituted sample shows a slightly diminished low-temperature reduction peak, while the higher-temperature peak becomes more pronounced and shifts toward a higher temperature range. In the Ca-substituted sample, the PtO_x-related low-temperature peak appears more intense and slightly upshifted, accompanied by a strong reduction peak in the higher-temperature region. In contrast, the Sr- and Ba-substituted samples display no noticeable low-temperature peaks associated with PtO_x reduction, suggesting a lower fraction of oxidized Pt species [32]. Instead, these samples show broad reduction features at higher temperatures, shifted toward lower temperature ranges compared to Mg and Ca analogues. These changes in the reduction profiles indicate that both the oxidation state of Pt and the interaction strength between lattice oxygen and the perovskite framework are significantly affected by A-site substitution. The absence of a distinct PtO_x peak in 1Pt/$LaSrFeO_3$ and 1Pt/$LaBaFeO_3$ samples implies a higher proportion of metallic Pt in the as-prepared state (Fig. 4c). Furthermore, the low-temperature-shifted reduction behavior of the perovskite samples suggests weaker metal–oxygen bonding, possibly accompanied by an increased concentration of oxygen vacancies. It should be noted that Pt appears to be well dispersed as a small

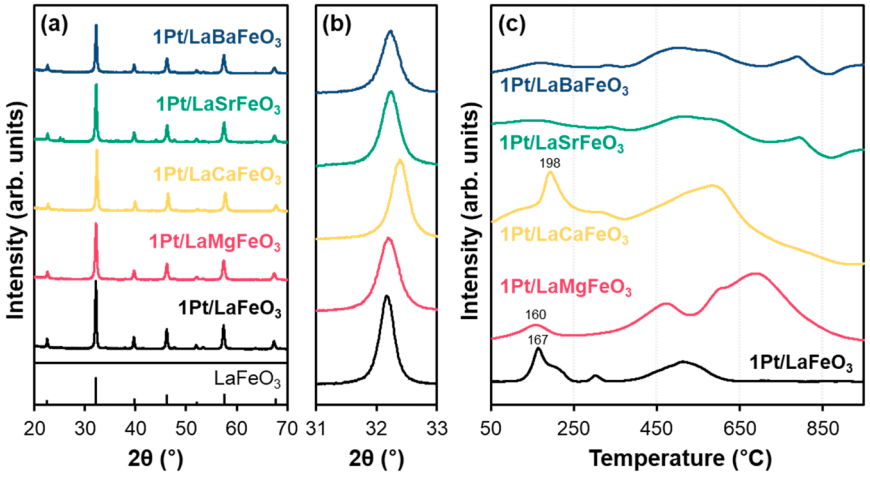

Fig. 4. (a) XRD patterns and (b) their magnified view in the 2θ region of 31–33° of 1Pt/$La_{0.8}A_{0.2}FeO_3$ (A = Mg, Ca, Sr, and Ba) with 1Pt/$LaFeO_3$ and vertical (hkl) lines indicating peaks corresponding to $LaFeO_3$ perovskite from the JCPDS database. (c) H_2-TPR profiles of 1Pt/$La_{0.8}A_{0.2}FeO_3$ series with 1Pt/$LaFeO_3$.

nanoparticle over the perovskite surface. However, the Ca-substituted sample exhibits slight aggregation of Pt particles as shown in the TEM images of the 1 wt% Pt-impregnated $La_{0.8}A_{0.2}FeO_3$ perovskites (Fig. 5).

3.2. Aerobic oxidation of ethylene glycol

It is generally known that various products could be formed via various reaction pathways during the aerobic oxidation of EG (Scheme 1). The catalytic activity of the synthesized $1Pt/LaBO_3$ (B = Cr, Mn, Fe, and Co) series was evaluated for the selective oxidation of EG to GA, with the results presented in Fig. 6 and Table 2. A blank test conducted in the presence of NaOH but without a catalyst confirmed negligible EG conversion, emphasizing the necessity of catalytic activation. Among the $1Pt/LaBO_3$ catalysts, $1Pt/LaCrO_3$ exhibited the highest EG conversion (52.5 %), followed by $1Pt/LaFeO_3$ (31.3 %) and $1Pt/LaMnO_3$ (23.7 %), while $1Pt/LaCoO_3$ showed the lowest conversion at only 5.9 %. Regardless of EG conversion levels, all tested catalysts—including the blank—exhibited over 80 % selectivity toward glycolic acid, accompanied by minor amounts of oxalic acid (OA) and formic acid (FA) as byproducts. These results indicate the essential contribution of the catalyst to the overall reaction efficiency, especially EG conversion.

To further explore and enhance structure-dependent reactivity, a series of A-site-substituted perovskites, $1Pt/La_{0.8}A_{0.2}BO_3$, were prepared and tested (Figs. 7 and S9). While the overall product distribution remained largely consistent—dominated by GA with minor amounts of OA and FA—the EG conversion showed notable variation depending on both A-site and the B-site cations. In the Cr-based series (Fig. S9), the Ba-substituted perovskite exhibited the greatest improvement in EG conversion, increasing from 52.5 % for the parent $1Pt/LaCrO_3$ to 67.3 %. The $1Pt/La_{0.8}Mg_{0.2}CrO_3$ catalyst also showed moderate enhancement, with a conversion of 58.4 %. In contrast, Ca- and Sr-substituted perovskites exhibited decreased activity, with EG conversions of 33.6 % and 49.3 %, respectively. The Fe-based series (Fig. 7), by comparison, exhibited a more pronounced dependence on A-site composition. Notably, $1Pt/La_{0.8}Sr_{0.2}FeO_3$ and $1Pt/La_{0.8}Ba_{0.2}FeO_3$ showed significant improvements in EG conversion, reaching 95.8 % and 86.2 %, respectively—substantially higher than that of the parent $1Pt/LaFeO_3$ catalyst (31.3 %). The Mg-substituted sample showed a marginal increase to 39.1 %, whereas $1Pt/La_{0.8}Ca_{0.2}FeO_3$ exhibited even lowered activity with 27.6 % of EG conversion, falling below that of the unmodified counterpart.

To assess the practical applicability of the most active $1Pt/La_{0.8}A_{0.2}FeO_3$ (A = Mg, Ca, Sr, and Ba) catalysts, EG oxidation was further evaluated under mild conditions using atmospheric pressure and continuous O_2 bubbling, instead of the previously employed pressurized batch system, with the results shown in Fig. 8 and Fig. S10. As expected, overall conversion levels were lower than those under pressurized conditions, but the relative activity trend was maintained. The Sr-substituted catalyst ($1Pt/La_{0.8}Sr_{0.2}FeO_3$) exhibited the highest performance, achieving over 50 % EG conversion within 8 h with continuous improvement over time. The Ba-substituted catalyst ($1Pt/La_{0.8}Ba_{0.2}FeO_3$) also showed notable activity, although slightly lower than $1Pt/La_{0.8}Sr_{0.2}FeO_3$, and displayed a saturation trend after 4 h. In contrast, the parent $1Pt/LaFeO_3$ catalyst, along with the Mg- and Ca-substituted counterparts, exhibited limited activity, with EG conversions barely exceeding 10 % and reaching a plateau within the first 2 h. Notably, GA selectivity remained high across all samples, regardless of the A-site substitution, which is consistent with the previous findings under high-pressure conditions. Sr- and Ba-substituted catalysts not only perform well under optimized batch conditions but also retain considerable activity under milder, more practical environments. The enhanced performance of these catalysts highlights the potential of A-site engineering with alkaline earth metals as an effective strategy to tune catalytic behavior in EG oxidation. However, the exact reasons behind these improvements in performance still need to be explained. Given the remarkable activity improvements observed in the Fe-based series, these catalysts were selected for further investigation. The following section focuses on elucidating the structure–activity relationship through detailed physicochemical characterization.

3.3. Origin of catalytic performance

To understand the factors governing the catalytic performance of the $1Pt/La_{0.8}A_{0.2}FeO_3$ (A = Mg, Ca, Sr, and Ba) series in EG oxidation, surface chemical states and redox properties were investigated using XPS, O_2-TPO-MS, and ethanol chemisorption measurements. XPS was

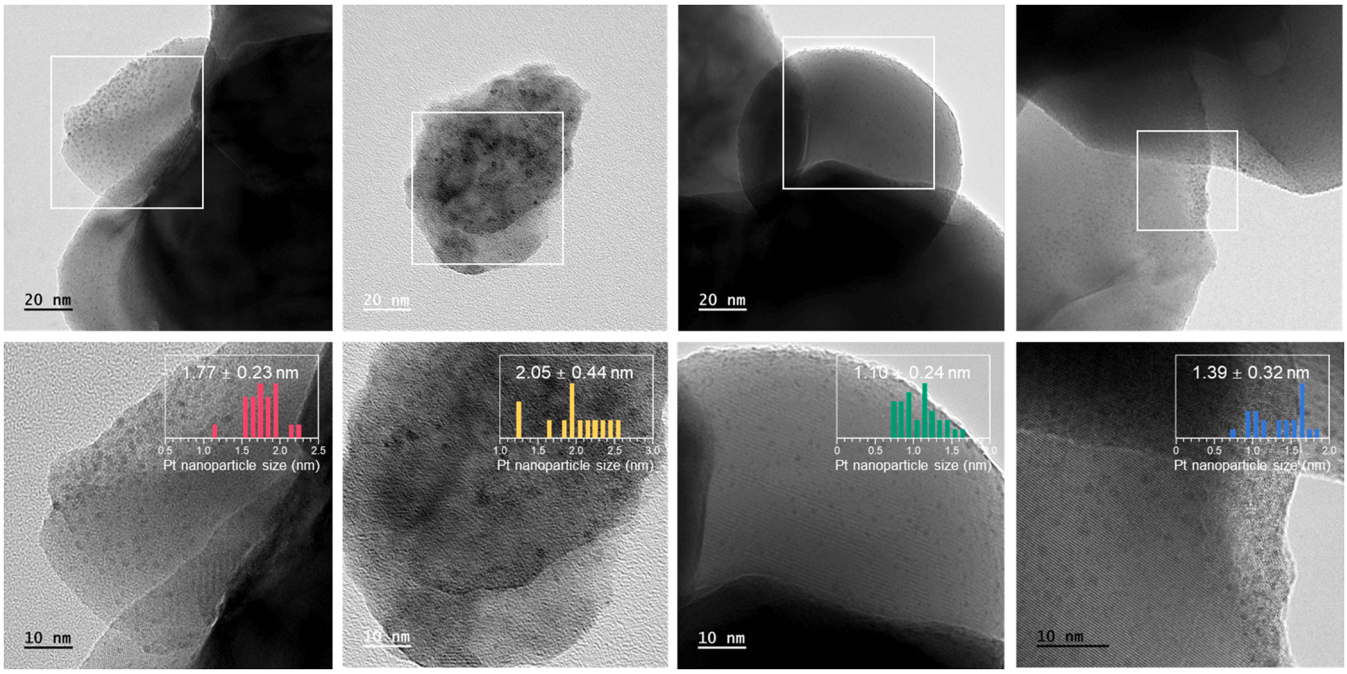

Fig. 5. TEM images of $La_{0.8}A_{0.2}FeO_3$ (A = Mg, Ca, Sr, and Ba) with magnified view (bottom row) and the corresponding histograms of Pt nanoparticle size distribution. (a) $1Pt/La_{0.8}Mg_{0.2}FeO_3$, (b) $1Pt/La_{0.8}Ca_{0.2}FeO_3$, (c) $1Pt/La_{0.8}Sr_{0.2}FeO_3$, and (d) $1Pt/La_{0.8}Ba_{0.2}FeO_3$.

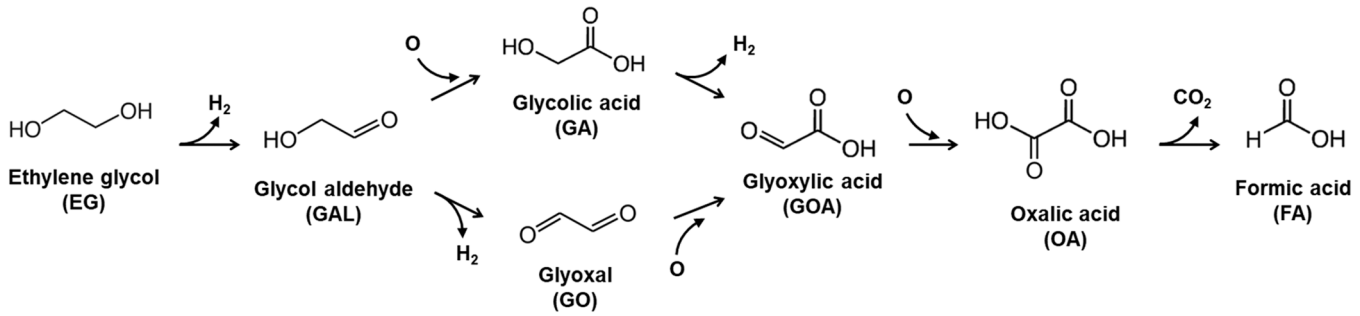

Scheme 1. Schematic representation showing the aerobic oxidation of EG to various products via various reaction pathways. The proposed corresponding chemical equations of aerobic oxidation of EG to each product were presented in Supplementary material.

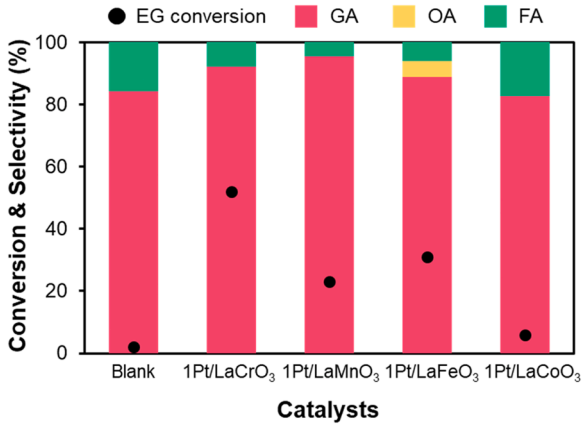

Fig. 6. Ethylene glycol conversion reaction results showing EG conversion (black circle) and product selectivity (bar graph with different colors: glycolic acid (GA) in red, oxalic acid (OA) in yellow, and formic acid (FA) in green) of $1Pt/LaBO_3$ (B = Cr, Mn, Fe, and Co) series with blank test. Detailed values obtained during the reaction were summarized in Table 2.

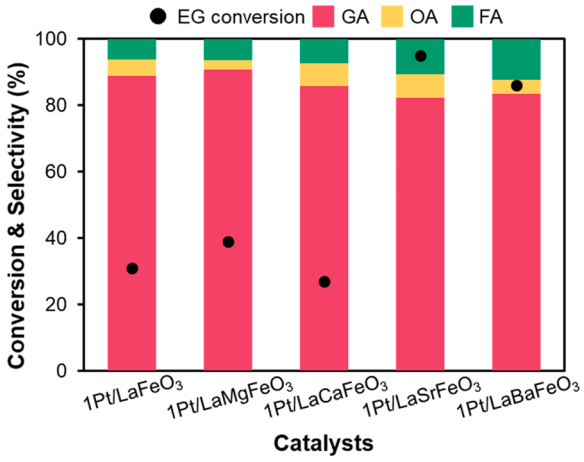

Fig. 7. Ethylene glycol conversion reaction results showing EG conversion (black circle) and product selectivity (bar graph with different colors: glycolic acid (GA) in red, oxalic acid (OA) in yellow, and formic acid (FA) in green) of $1Pt/La_{0.8}A_{0.2}FeO_3$ series. Detailed values obtained during the reaction were summarized in Table 3.

Table 2
Catalytic performance of oxidation of EG using $1Pt/LaBO_3$ series.

Catalyst	EG Conversion (%)	Product Selectivity (%)			Carbon Balance (%)
		GA	OA	FA	
Blank	2.1	84.3	0	15.7	82.1
$1Pt/LaCrO_3$	52.5	92.2	0	7.8	75.5
$1Pt/LaMnO_3$	23.7	95.5	0	4.5	79.8
$1Pt/LaFeO_3$	31.3	88.8	5.1	6.1	78.2
$1Pt/LaCoO_3$	5.9	82.6	0	17.4	81.6

employed to analyze the surface states of platinum, lanthanum, the alkaline earth metals, iron, oxygen, and carbon under reduced condition. The results are summarized in Fig. 9, Fig. S11, and Table S6.

XPS analysis of the Pt 4 f region confirmed the presence of both metallic Pt^0 and oxidized Pt^{2+} species across all samples, but the relative proportions and binding energies of these components varied depending on the A-site substitution (Fig. 9a). A comparison of the Pt^0/Pt^{2+} ratios reveals that the Sr- and Ba-substituted catalysts possess the highest fractions of metallic Pt, at 81.2 % and 82.0 %, respectively. In contrast, the Ca-substituted sample exhibited a moderate concentration with 68.8 %, while the Mg-substituted and parent $LaFeO_3$ catalysts showed significantly lower metallic Pt concentrations of 58.1 % and 56.0 %, respectively. Most samples displayed Pt^0 4 $f_{7/2}$ peaks centered at 71.3–71.4 eV; however, the Mg-substituted sample exhibited a slightly lower binding energy at 71.1 eV, suggesting subtle differences in the local electronic environment of Pt.

Previous studies have demonstrated that metallic Pt^0 is the intrinsic active species for the oxidation of EG [32]. For instance, Pt/NaY catalysts were shown to enhance EG oxidation activity via a unique $(Si–OH)_n$–Pt interface that stabilizes Pt^0 species and facilitates σ-bond activation pathways [32]. Similarly, Pt/HAP systems revealed that isolated metallic Pt sites, rather than aggregated Pt–Pt ensembles, serve as effective active sites for EG-to-GA conversion [33]. Consistent with these findings, our study also observed a strong correlation between the Pt^0/Pt^{2+} (summarized in Table S6) and catalytic activity (Fig. 9c), suggesting that higher metallic Pt content is a key factor governing the enhanced conversion of EG. These results align with the established understanding that σ-bond activation of C–H and O–H bonds by metallic Pt^0 plays a dominant role in the oxidative dehydrogenation step [34].

The O 1 s XPS spectra of the $1Pt/La_{0.8}A_{0.2}FeO_3$ series were analyzed to examine the surface oxygen species and their relation to catalytic behavior (Fig. 9b). All spectra were deconvoluted into three components: lattice oxygen (O_{latt}), oxygen vacancy-related species (O_{vac}), and surface hydroxyl or adsorbed oxygen species (O_{OH}) [39,42–44]. Among the catalysts, the Sr- and Ba-substituted samples exhibited the highest O_{vac} proportions, at 44.6 % and 42.7 %, respectively (Table S6), followed by Mg-substituted sample with 39.3 %, non-substituted $LaFeO_3$ sample with 38.9 %, and the Ca-substituted sample with the lowest value of 35.2 %. In contrast, the O_{latt} fractions were lower in the Sr-substituted (53.7 %) and Ba-substituted (55.2 %) samples than in Ca-substituted (62.4 %), non-substituted $LaFeO_3$ (58.7 %), and Mg-substituted (56.1 %) samples, further indicating a relative increase in oxygen defect content. Additionally, the Sr- and Ba-substituted samples displayed a slight shift in the overall O 1 s binding energy toward

Table 3
Catalytic performance of oxidation of EG using $1Pt/La_{0.8}A_{0.2}FeO_3$ series.

Catalyst	EG Conversion (%)	Product Selectivity (%)					Carbon Balance (%)
		GA	GO	GOA	OA	FA	
$1Pt/LaFeO_3$	31.3	88.8	0	0	5.1	6.1	78.2
$1Pt/La_{0.8}Mg_{0.2}FeO_3$	39.1	90.8	0	0	2.7	6.5	82.5
$1Pt/La_{0.8}Ca_{0.2}FeO_3$	27.6	85.9	0	0	6.8	7.3	83.1
$1Pt/La_{0.8}Sr_{0.2}FeO_3$	95.8	82.2	0	0	7.1	10.7	88.2
$1Pt/La_{0.8}Ba_{0.2}FeO_3$	86.2	83.4	0	0	4.2	12.4	87.3

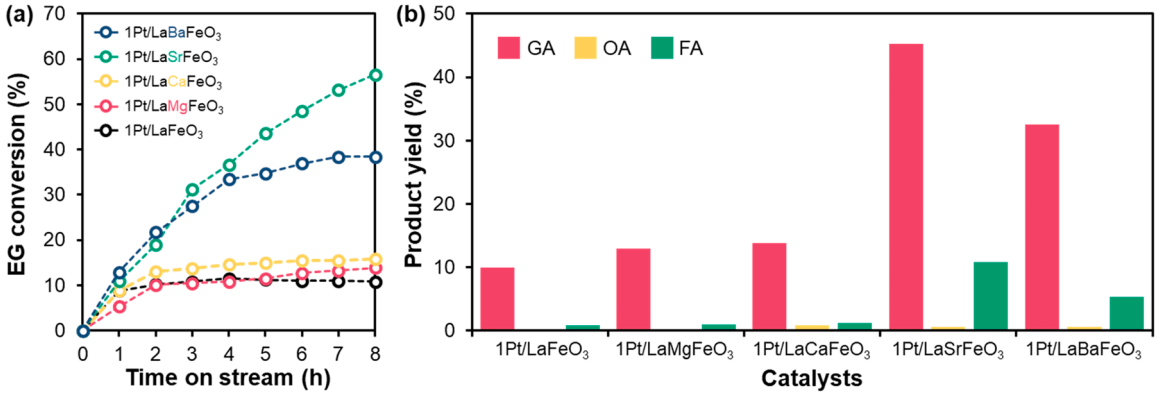

Fig. 8. Atmospheric-pressure EG conversion reaction results showing (a) EG conversion as a function of time on stream (h) and (b) product yield during the 8-hour reaction using the $1Pt/La_{0.8}A_{0.2}FeO_3$ (A = Mg, Ca, Sr, and Ba) series in comparison with $1Pt/LaFeO_3$. Detailed reaction profiles were presented in Fig. S10.

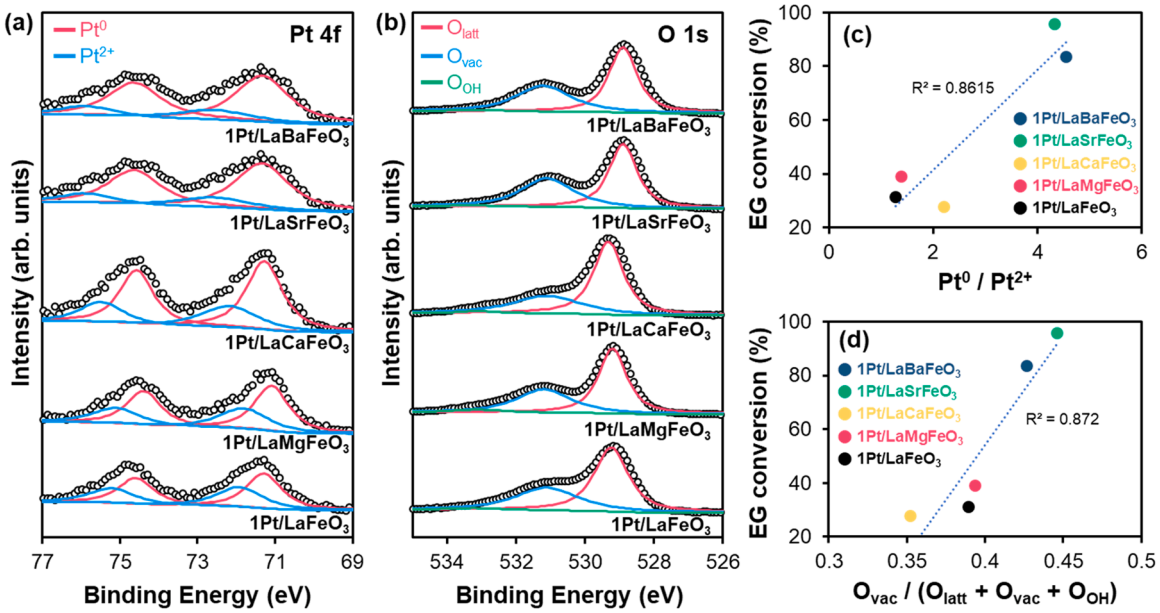

Fig. 9. XPS spectra in the binding energy regions of (a) Pt 4 f and (b) O 1 s of $1Pt/La_{0.8}A_{0.2}FeO_3$ series with $1Pt/LaFeO_3$. Relationships between EG conversion and values of (c) Pt^0 / Pt^{2+} ratio and (d) O_{vac} / (O_{latt} + O_{vac} + O_{OH}) (see Table S6).

lower values (Fig. 9b), which may reflect weaker metal–oxygen interactions or an increase in electron-rich oxygen vacancy sites [47]. These features are indicative of enhanced oxygen mobility and surface reactivity. A plot of O_{vac} concentration (i.e., O_{vac} / (O_{latt} + O_{vac} + O_{OH})) versus EG conversion (Fig. 9d) reveals a positive correlation: catalysts with a greater concentration of surface oxygen vacancies exhibit higher catalytic activity. This trend supports the hypothesis that oxygen vacancies facilitate O_2 activation under reaction conditions, thereby accelerating key steps in the oxidation of EG. In addition to Pt and O, the XPS spectra of La 3 d, Fe 2p, and the respective alkaline earth metals (Mg, Ca, Sr, Ba) were analyzed (Fig. S11). All samples exhibited binding energies consistent with La^{3+}, Fe ion, and the expected oxidation states of the A-site dopants, in agreement with those typically reported for well-defined perovskite structures [38,40,43,45]. No significant variation was observed among the samples, indicating that A-site substitution had minimal impact on the electronic states of the framework cations.

To evaluate the actual oxygen activation ability of the catalysts under reaction-relevant conditions, O_2-TPO-MS experiments were conducted (Fig. 10). The Sr-substituted sample exhibited a distinct oxygen consumption peak centered around 250 °C, indicating a high degree of reactivity with molecular oxygen. The Ba-substituted sample also showed a noticeable but slightly less intense peak in the same

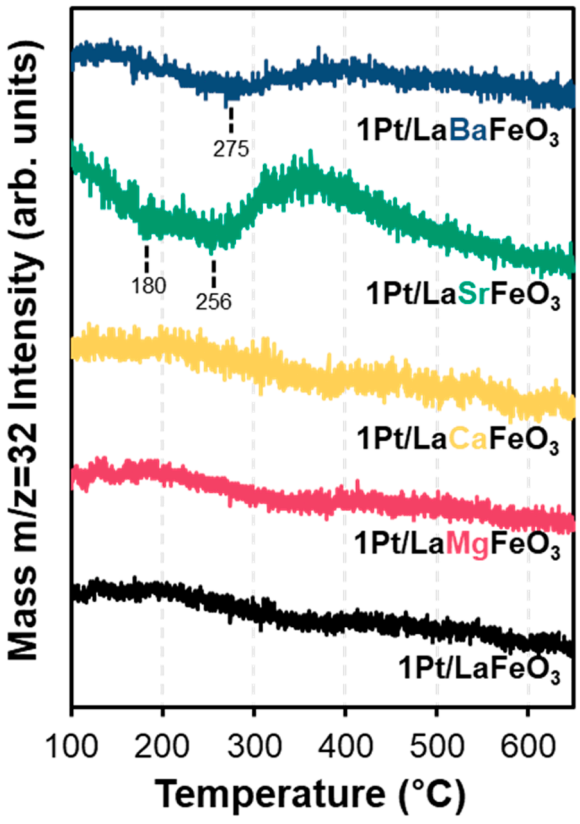

Fig. 10. Mass ($m/z = 32$) profiles of $1Pt/La_{0.8}A_{0.2}FeO_3$ (A = Mg, Ca, Sr, and Ba) series in comparison with $1Pt/LaFeO_3$ during O_2-TPO-MS analysis.

temperature range. In contrast, the Mg- and Ca-substituted samples displayed negligible O_2 consumption throughout the temperature range, suggesting limited ability to activate gaseous oxygen. These results align well with the higher oxygen vacancy concentrations identified in XPS and the superior catalytic performance observed for the Sr- and Ba-substituted catalysts. The enhanced O_2 uptake under thermal conditions further supports that A-site substitution with Sr or Ba enhances surface oxygen dynamics, thereby contributing to the superior performance in EG oxidation. It should be noted that the TPO-MS experiments were also conducted for the $1Pt/La_{0.8}A_{0.2}CrO_3$ series (Fig. S12); however, no distinct peak was observed. We hypothesized that A-site substitution induces lattice distortion in the perovskite structure, thereby modulating the electronic properties of the support. These changes likely influence the strength of Pt–support interactions and the mobility of surface oxygen species, as evidenced by XPS and O_2-TPO results. However, we acknowledge that a fundamental understanding of why Sr substitution in $LaFeO_3$ results in superior performance—while Sr substitution in $LaCrO_3$ or Ca substitution in $LaFeO_3$ does not—remains unclear. This study primarily focused on catalyst screening and evaluation of reaction performance, and therefore does not fully elucidate the mechanistic origins of the observed differences. Further in-depth studies are planned to investigate the structural and electronic factors governing these variations.

Ethanol chemisorption analysis revealed notable differences in Pt dispersion across the $1Pt/La_{0.8}A_{0.2}FeO_3$ (A = Mg, Ca, Sr, and Ba) catalyst series (Fig. S13 and Table 4). In fact, we carried out CO and H_2 chemisorption analyses, but strong interactions between the probe molecules and the perovskite supports interfered the accurate quantification of Pt dispersion. Instead, ethanol chemisorption could reliably be used for quantification of Pt dispersion in this case, as reported in literatures [31, 48,49]. While the $LaFeO_3$, and its corresponding Mg- and Ca-substituted samples exhibited similar Pt dispersion values ranging from 41.7 % to 47.1 %, the Sr- and Ba-substituted catalysts showed slightly higher dispersions of 52.4 % and 50.2 %, respectively (Table 4). These relatively enhanced values suggest improved Pt surface accessibility in the Sr- and Ba-substituted systems, which may contribute to their superior catalytic activity. The corresponding average Pt particle sizes, calculated from the chemisorption data, support this trend. The Sr- and Ba-substituted samples featured the smallest Pt nanoparticles, with diameters of 2.16 nm and 2.25 nm, respectively, whereas larger particles were observed for $LaFeO_3$ (2.50 nm), Mg (2.40 nm), and Ca (2.71 nm) counterparts (Table 4). These results imply that A-site substitution with Sr or Ba can effectively suppress Pt agglomeration, likely by modifying the metal–support interface in a way that favors the stabilization of finely dispersed Pt species.

Table 4
Pt dispersion and particle size of $1Pt/La_{0.8}A_{0.2}FeO_3$ series determined through ethanol pulse adsorption.

Catalyst	Dispersion (%)	Particle Size (nm)
$1Pt/LaFeO_3$	45.3	2.50
$1Pt/La_{0.8}Mg_{0.2}FeO_3$	47.1	2.40
$1Pt/La_{0.8}Ca_{0.2}FeO_3$	41.7	2.71
$1Pt/La_{0.8}Sr_{0.2}FeO_3$	52.4	2.16
$1Pt/La_{0.8}Ba_{0.2}FeO_3$	50.2	2.25

Notably, beyond quantifying Pt dispersion, ethanol chemisorption offers additional insight into the surface reactivity of catalyst. Since both ethanol and ethylene glycol contain hydroxyl (–OH) groups, the extent of ethanol adsorption can serve as an indirect indicator of how readily the catalyst interacts with the actual reactant, EG. In this context, the enhanced ethanol uptake observed for the Sr- and Ba-substituted catalysts may also reflect a higher affinity for EG molecules, contributing to their superior oxidation performance. Thus, ethanol chemisorption not only reveals physical dispersion characteristics but also provides a qualitative basis for comparing surface–reactant interactions among different catalyst systems.

4. Conclusions

In this study, we systematically investigated the influence of structural composition in La-based perovskite oxides (ABO_3) on the catalytic performance of Pt-supported materials for the selective oxidation of EG to GA. We prepared A-metal and B-metal controlled perovskite series via the co-precipitation method, and 1 wt% Pt was impregnated to generate catalytically active sites. Through a B-site screening in $1Pt/LaBO_3$ perovskites, $LaCrO_3$ and $LaFeO_3$ were identified as promising supports for EG oxidation. Furthermore, partial A-site substitution in $LaFeO_3$ confirmed that A-site modification induced subtle changes in the perovskite lattice without disrupting the overall framework, but it demonstrated that Sr-substituted $1Pt/La_{0.8}Sr_{0.2}FeO_3$ catalysts exhibited significantly enhanced EG conversion while maintaining high GA selectivity, even under mild atmospheric conditions. XPS analysis demonstrated that $1Pt/La_{0.8}Sr_{0.2}FeO_3$ perovskite possessed a higher proportion of metallic Pt^0 species and greater surface oxygen vacancy concentrations. O_2-TPO measurements supported this by showing distinct low-temperature O_2 consumption, indicative of improved oxygen activation ability. Ethanol pulse adsorption experiments further confirmed superior Pt dispersion and smaller particle sizes in $1Pt/La_{0.8}Sr_{0.2}FeO_3$ perovskite, which likely contributed to the enhanced performance. The observed ethanol uptake also suggested a higher affinity for –OH functional groups, potentially promoting EG adsorption and facilitating reaction kinetics. These findings highlight the synergistic effects between perovskite composition and supported Pt species, where A- and B-site engineering plays a key role in modulating redox behavior and metal–support interaction. This work not only presents a viable strategy for optimizing noble metal-based catalysts in biomass-derived polyol oxidation but also offers valuable insights for the rational design of advanced materials in selective oxidation chemistry.

CRediT authorship contribution statement

Seungdon Kwon: Writing – review & editing, Writing – original draft, Investigation, Data curation. **Nagyeong Kim:** Investigation, Data curation. **Hyeonji Yeom:** Investigation, Data curation. **Hanbit Jang:** Investigation, Data curation. **Kyungsu Na:** Writing – review & editing, Writing – original draft, Supervision, Project administration, Investigation, Funding acquisition, Data curation, Conceptualization.

Declaration of Competing Interest

The authors declare that they have no known competing financial interests or personal relationships that could have appeared to influence the work reported in this paper.

Acknowledgements

This work was supported by the National Research Foundation of Korea (NRF) grant funded by the Korea government (MSIT) (RS-2024–00349276).

Appendix A. Supporting information

Supplementary data associated with this article can be found in the online version at doi:10.1016/j.cattod.2025.115548

Data availability

All data are available in the main text or the supplementary materials.

References

[1] L. Chen, C. Msigwa, M. Yang, A.I. Osman, S. Fawzy, D.W. Rooney, P. Yap, Strategies to achieve a carbon neutral society:a review, Environ. Chem. Lett. 20 (2022) 2277–2310, https://doi.org/10.1007/s10311-022-01435-8.
[2] T. Khandaker, T. Islam, A. Nandi, M.A.A.M. Anik, M.S. Hossain, M.K. Hasan, M. S. Hossain, Biomass-derived carbon materials for sustainable energy applications: a comprehensive review, Sustain. Energy Fuels 9 (2025) 693–723, https://doi.org/10.1039/D4SE01393J.
[3] S. Rajendran, A. Al-Samydai, G. Palani, H. Trilaksana, T. Sathish, J. Giri, R. Saravanan, J.I.J. Lalvani, F. Nasri, Replacement of petroleum based products with Plant-Based materials, Green and sustainable Energy—A review, Eng. Rep. 7 (2025) e70108, https://doi.org/10.1002/eng2.70108.
[4] R.R. Nayak, N.K. Gupta, Renewable aromatic production from waste: exploring pathways, source materials, and catalysts, Green. Chem. 27 (2025) 8055–8111, https://doi.org/10.1039/D4GC05683C.
[5] M.S. Akhtar, M.T. Naseem, S. Ali, W. Zaman, Metal-Based catalysts in biomass transformation: from plant feedstocks to renewable fuels and chemicals, Catalysts 15 (2025) 40, https://doi.org/10.3390/catal15010040.
[6] P. Sudarsanam, R. Zhong, S.V.D. Bosch, S.M. Coman, V.I. Parvulescu, B.F. Sels, Functionalised heterogeneous catalysts for sustainable biomass valorisation, Chem. Soc. Rev. 47 (2018) 8349–8402, https://doi.org/10.1039/c8cs00410b.
[7] L.R. Lynd, G.T. Beckham, A.M. Guss, L.N. Jayakody, E.M. Karp, C. Maranas, R. L. McCormick, D. Amador-Noguez, Y.J. Bomble, B.H. Davison, C. Foster, M. E. Himmel, E.K. Holwerda, M.S. Laser, C.Y. Ng, D.G. Olson, Y. Roman-Leshkov, C. T. Trinh, G.A. Tuskan, V. Upadhayay, D.R. Vardon, L. Wangaf, C.E. Wyman, Toward low-cost biological and hybrid biological/ catalytic conversion of cellulosic biomass to fuels, Energy Environ. Sci. 15 (2022) 938–990, https://doi.org/10.1039/d1ee02540f.
[8] X. Liu, X. Wang, S. Yao, Y. Jiang, J. Guana, X. Mu, Recent advances in the production of polyols from lignocellulosic biomass and biomass-derived compounds, RSC Adv. 4 (2014) 49501–49520, https://doi.org/10.1039/c4ra06466f.
[9] C. Xu, E. Paone, D. Rodríguez-Padron, R. Luque, F. Mauriello, Reductive catalytic routes towards sustainable production of hydrogen, fuels and chemicals from biomass derived polyols, Renew. Sust. Energ. Rev. 127 (2020) 109852, https://doi.org/10.1016/j.rser.2020.109852.
[10] J. Sun, H. Liu, Selective hydrogenolysis of biomass-derived xylitol to ethylene glycol and propylene glycol on supported ru catalysts, Green. Chem. 13 (2011) 135–142, https://doi.org/10.1039/c0gc00571a.
[11] Y. Zhang, F. Xu, F. Chen, Y. Zhang, Y. Wu, L. Jiang, Dual utilization of lignocellulose biomass and glycerol waste to produce fermentable levoglucosan via fast pyrolysis, Front. Chem. 10 (2022) 847767, https://doi.org/10.3389/fchem.2022.847767.
[12] M.K. Wong, S.S.M. Lock, Y.H. Chan, S.J. Yeoh, I.S. Tan, Towards sustainable production of bio-based ethylene glycol: progress, perspective and challenges in catalytic conversion and purification, Chem. Eng. J. 468 (2023) 143699, https://doi.org/10.1016/j.cej.2023.143699.
[13] G.D. Yadav, P.A. Chandan, A Green process for glycerol valorization to glycerol carbonate over heterogeneous hydrotalcite catalyst, Catal. Today 237 (2014) 47–53, https://doi.org/10.1016/j.cattod.2014.01.043.
[14] L. Vilcocqa, A. Cabiac, C. Especel, S. Lacombea, D. Duprez, Hydrocarbon fuel synthesis from sorbitol over bifunctional catalysts: association of tungstated titania with platinum, palladium or iridium, Catal. Today 242 (2015) 91–100, https://doi.org/10.1016/j.cattod.2014.06.014.
[15] S. Liu, Y. Okuyama, M. Tamura, Y. Nakagawa, A. Imai, K. Tomishigea, Catalytic conversion of sorbitol to gasoline-ranged products without external hydrogen over Pt-modified Ir-ReO_x/SiO_2, Catal. Today 269 (2016) 122–131, https://doi.org/10.1016/j.cattod.2015.10.023.
[16] M. Elsayed, M. Eraky, A.I. Osman, J. Wang, M. Farghali, A.K. Rashwan, I. H. Yacoub, D. Hanelt, A. Abomohra, Sustainable valorization of waste glycerol into bioethanol and biodiesel through biocircular approaches: a review, Environ. Chem. Lett. 22 (2024) 609–634, https://doi.org/10.1007/s10311-023-01671-6.
[17] F.D.S. Pereira, V.F. de Santana, A.C.A. Silva, A. Tofanello, P.N. Romano, J.M.A. R. de Almeida, T.S. Rodrigues, I.D.A. Rodrigues, R.B. de Lima, M.A.S. Garcia, Electrooxidation of ethylene glycol using Ag-Pt nanotubes supported on silica: correlating the unexpected O-vacancies creation with catalytic performance, Catal. Today 441 (2024) 114914, https://doi.org/10.1016/j.cattod.2024.114914.
[18] M.P. Urrea, F. Herold, D. Chen, M. Rønning, Nitrogen-containing carbon nanofibers as supports for bimetallic Pt-Mn catalysts in aqueous phase reforming of ethylene glycol, Catal. Today 418 (2023) 114066, https://doi.org/10.1016/j.cattod.2023.114066.
[19] H. Yue, Y. Zhao, X. Ma, J. Gong, Ethylene glycol: properties, synthesis, and applications, Chem. Soc. Rev. 41 (2012) 4218–4244, https://doi.org/10.1039/c2cs15359a.
[20] X. Gu, B. Liu, J. Greeley, First-Principles study of structure sensitivity of ethylene glycol conversion on platinum, ACS Catal. 5 (2015) 2623–2631, https://doi.org/10.1021/cs5019088.
[21] D. Mei, V.L. Dagle, R. Xing, K.O. Albrecht, R.A. Dagle, Steam reforming of ethylene glycol over $MgAl_2O_4$ supported rh, ni, and co catalysts, ACS Catal. 6 (2016) 315–325, https://doi.org/10.1021/acscatal.5b01666.
[22] G.W. Huber, J.W. Shabaker, S.T. Evans, J.A. Dumesic, Aqueous-phase reforming of ethylene glycol over supported pt and pd bimetallic catalysts, Appl. Catal. B Environ. 62 (2006) 226–235, https://doi.org/10.1016/j.apcatb.2005.07.010.
[23] Z. Li, B.D. Kay, Z. Dohnalek, Dehydration and dehydrogenation of ethylene glycol on rutile TiO_2(110), Phys. Chem. Chem. Phys. 15 (2013) 12180–12186, https://doi.org/10.1039/c3cp50687h.
[24] F. Cui, S. Huang, R. Jin, H. Cui, X. Wu, Y. Dai, M. Guo, G. He, Integration of a well-designed biomass pair in electrochemical hydrogen pump reactor: ethylene glycol dehydrogenation and levulinic acid hydrogenation, Int. J. Hydrog. Energy 47 (2022) 28086–28094, https://doi.org/10.1016/j.ijhydene.2022.06.129.
[25] N.L. Chauhana, V. Dameeraa, A. Chowdhury, V.A. Juvekar, A. Sarkar, Electrochemical oxidation of ethylene glycol in a channel flow reactor, Catal. Today 309 (2018) 126–132, https://doi.org/10.1016/j.cattod.2017.08.053.
[26] L. Prati1, M. Rossi, Gold on carbon as a new catalyst for selective liquid phase oxidation of diols, J. Catal. 176 (1998) 552–560, https://doi.org/10.1006/jcat.1998.2078.
[27] C. Bianchi, F. Porta, L. Prati, M. Rossi, Selective liquid phase oxidation using gold catalysts, Top. Catal. 13 (2000) 231–236, https://doi.org/10.1023/A:1009065812889.
[28] H. Shi, X. Yin, B. Subramaniam, R.V. Chaudhari, Liquid-Phase oxidation of ethylene glycol on pt and Pt−Fe catalysts for the production of glycolic acid: remarkable bimetallic effect and reaction mechanism, Ind. Eng. Chem. Res. 58 (2019) 18561–18568, https://doi.org/10.1021/acs.iecr.9b03419.
[29] M.B. Griffin, A.A. Rodriguez, M.M. Montemore, J.R. Monnier, C.T. Williams, J. W. Medlin, The selective oxidation of ethylene glycol and 1,2-propanediol on au, pd, and Au–Pd bimetallic catalysts, J. Catal. 307 (2013) 111–120, https://doi.org/10.1016/j.jcat.2013.07.012.
[30] S. Tschirner, E. Weingart, L. Teevs, U. Prüße, Oxidation of monoethylene glycol to glycolic acid with Gold-Based catalyst and glycolic acid isolation by electrodialysis, Reactions 3 (2022) 47–58, https://doi.org/10.3390/reactions3010004.
[31] H. Yan, S. Yao, J. Wang, S. Zhao, Y. Sun, M. Liu, X. Zhou, G. Zhang, X. Jin, X. Feng, Y. Liu, X. Chen, D. Chen, C. Yang, Engineering Pt-Mn_2O_3 interface to boost selective oxidation of ethylene glycol to glycolic acid, Appl. Catal. B Environ. 284 (2021) 119803, https://doi.org/10.1016/j.apcatb.2020.119803.
[32] F. Du, Z. You, K. Meng, X. Qu, D. Zhang, W. Zhang, M. Liu, Y. Shen, W. Deng, X. Jin, Dealuminization for a modified $(Si-OH)_n$−Pt interface: Self-Activation of Pt/NaY catalysts for oxidation of ethylene glycol in a Base-Free medium, ACS Sustain. Chem. Eng. 9 (2021) 14416–14429, https://doi.org/10.1021/acssuschemeng.1c04448.
[33] H. Yan, M. Zhao, X. Feng, S. Zhao, X. Zhou, S. Li, M. Zha, F. Meng, X. Chen, Y. Liu, D. Chen, N. Yan, C. Yang, PO_4^{3-} coordinated robust Single-Atom platinum catalyst for selective polyol oxidation, Angew. Chem. Int. Ed. 61 (2022) e202116059, https://doi.org/10.1002/anie.202116059.
[34] N. Mota, I.Z. Ismagilov, E.V. Matus, V.V. Kuznetsov, M.A. Kerzhentsv, Z. R. Ismagilov, R.M. Navarro, J.L.G. Fierro, Hydrogen production by autothermal reforming ofmethane over lanthanum chromites modified with ru and sr, Int. J. Hydrog. Energy 41 (2016) 19373–19381, https://doi.org/10.1016/j.ijhydene.2016.05.029.

[35] G. Peron, A. Glisenti, Perovskites as alternatives to noble metals in automotive exhaust abatement: activation of oxygen on $LaCrO_3$ and $LaMnO_3$, Top. Catal. 62 (2019) 244–251, https://doi.org/10.1007/s11244-018-1120-1.
[36] F. Pan, W. Zhang, C. Ferronato, J.L. Valverde, A. Giroir-Fendler, Boosting propene oxidation activity over LaFeO3 perovskite catalysts by cobalt substitution, Appl. Catal. AGen. 643 (2022) 118779, https://doi.org/10.1016/j.apcata.2022.118779.
[37] X. Yang, L. Yang, W. Fan, H. Lin, Effect of redox properties of $LaCoO_3$ perovskite catalyst on production of lactic acid from cellulosic biomass, Catal. Today 269 (2016) 56–64, https://doi.org/10.1016/j.cattod.2015.12.003.
[38] F. Li, P. Zhang, W. Zhang, D. Fang, K. Li, Activity trend and possible descriptor of $LaBO_3$ (B = Cr, Mn, Fe, Co) perovskite catalysts for electroreduction of nitrate, Chem. Eng. J. 472 (2023) 145148, https://doi.org/10.1016/j.cej.2023.145148.
[39] H. Yu, Y. Wang, X. Tao, F. Yu, T. Zhao, M. Li, Haiqian Wang, Interfacial Metal−Support interaction and catalytic performance of perovskite $LaCrO_3$-Supported ru catalyst, ACS Appl. Mater. Interfaces 16 (2024) 17483–17492, https://doi.org/10.1021/acsami.3c19119.
[40] S.B. Hammouda, F. Zhaoa, Z. Safaei, V. Srivastava, D.L. Ramasamya, S. Iftekhar, S. kalliola, M. Sillanpää, Degradation and mineralization of phenol in aqueous medium by heterogeneous monopersulfate activation on nanostructured cobalt based-perovskite catalysts $ACoO_3$ (A= La, Ba, Sr and Ce): characterization, kinetics and mechanism study, Appl. Catal. B Environ. 215 (2017) 60–73, https://doi.org/10.1016/j.apcatb.2017.05.051.
[41] D. Arias, A. Karelovic, C. Sepulveda, G. Pecchi, C. Herrera, Effect of the sr substitution in the A-site for $La_{1-x}Sr_xCoO_3$ perovskite catalysts for the valorization of levulinic acid to produce gamma-valerolactone, Catal. Today 450 (2025) 115210, https://doi.org/10.1016/j.cattod.2025.115210.
[42] J. Yang, L. Shi, L. Li, Y. Fang, C. Pan, Y. Zhu, Z. Liang, S. Hoang, Z. Li, Y. Guo, Surface modification of macroporous $La_{0.8}Sr_{0.2}CoO_3$ perovskite oxides integrated monolithic catalysts for improved propane oxidation, Catal. Today 376 (2021) 168–176, https://doi.org/10.1016/j.cattod.2020.06.043.
[43] N. Guo, L. Jiang, D. Wang, Y. Zhan, Z. Wang, Selective modulation of La-site vacancies in $La_{0.9}Ca_{0.1}MnO_3$ perovskites catalysts for toluene oxidation: the role of oxygen species on the catalytic mechanism, Sep. Purif. Technol. 310 (2023) 123227, https://doi.org/10.1016/j.seppur.2023.123227.
[44] Y. Zhu, Y. Sun, X. Niu, F. Yuan, H. Fu, Preparation of La-Mn-O perovskite catalyst by microwave irradiation method and its application to methane combustion, Catal. Lett. 135 (2010) 152–158, https://doi.org/10.1007/s10562-009-0034-8.
[45] X. Wu, M. Li, A. Abouserie, A. Frommelius, G. Dalfollo, T. Ohlerth, U. Simon, Acid treatment enhances the methane combustion activity of $LaFeO_3$ perovskite catalyst, Catal. Today 432 (2024) 114620, https://doi.org/10.1016/j.cattod.2024.114620.
[46] Y. Wu, T. Yu, B. Sheng, Dou, C. Wang, X. Xie, Z. Yu, S. Fan, Z. Fan, L. Wang, A comparative study on perovskite-type mixed oxide catalysts $A'xA1-xBO_{3-\lambda}$ (A′ = Ca, Sr, A = La, B = Mn, Fe, Co) for NH_3 oxidation, J. Catal. 120 (1989) 88–107, https://doi.org/10.1016/0021-9517(89)90253-4.
[47] H. Zhu, P. Zhang, S. Dai, Recent advances of Lanthanum-Based perovskite oxides for catalysis, ACS Catal. 5 (2015) 6370–6385, https://doi.org/10.1021/acscatal.5b01667.
[48] H. Yan, S. Yao, W. Liang, S. Zhao, X. Jin, X. Feng, Y. Liu, X. Chen, C. Yang, Ni–Co oxide catalysts with lattice distortions for enhanced oxidation of glycerol to glyceric acid, J. Catal. 381 (2020) 248–260, https://doi.org/10.1016/j.jcat.2019.11.001.
[49] L. G. Verga, A.E. Russell, C.-K. Skylaris, Ethanol, O, and CO adsorption on pt nanoparticles: effects of nanoparticle size and graphene support, Phys. Chem. Chem. Phys. 20 (2018) 25918–25930, https://doi.org/10.1039/c8cp04798g.